Ceramics International 43 (2017) 15288–15295

Contents lists available at ScienceDirect

Ceramics International

journal homepage: www.elsevier.com/locate/ceramint

Suspension high velocity oxy-fuel spraying of a rutile TiO_2 feedstock: Microstructure, phase evolution and photocatalytic behaviour

M. Bai, R. Khammas, L. Guan, J.W. Murray, T. Hussain*

Faculty of Engineering, University of Nottingham, NG7 2RD, UK

ARTICLE INFO

Keywords:
SHVOF
Rutile
Anatase
Microstructure
Phase evolution
Photocatalytic

ABSTRACT

Nano-structured TiO_2 coatings were produced by suspension high velocity oxy fuel (SHVOF) thermal spraying using water-based suspensions containing 30 wt% of submicron rutile powders (~180 nm). By changing the flame heat powers from 40 kW to 101 kW, TiO_2 coatings were obtained with distinctive microstructures, phases and photocatalytic behaviour. Spraying with low power (40 kW) resulted in a more porous microstructure with the presence of un-melted nano-particles and a lower content of the anatase phase; meanwhile, high powers (72/101 kW) resulted in denser coatings and rougher surfaces with distinctive humps but not necessarily with a higher content of anatase. Linear sweep voltammetry (LSV) was used to evaluate the photocatalytic performance. Surprisingly, coatings with the lowest anatase content (~20%) using 40 kW showed the best photocatalytic behaviour with the highest photo-conversion efficiency. It was suggested that this was partially owing to the increased specific surface area of the un-melted nano-particles. More importantly, the structural arrangement of the similarly sized TiO_2 nano-crystallites between rutile and antase phases also created catalytic "hot spots" at the rutile–anatase interface and greatly improved the photo-activity.

1. Introduction

TiO_2 exhibits good photo-catalytic properties for a wide range of applications, such as sensor devices, dye-sensitized solar cells, hydrogen evolution, solar energy harvesting and health care [1,2]. It is also generally believed that as a photo-catalyst, TiO_2 is more effective in the form of nano-particles, given their higher surface area [3,4]. By employing sub-micron or nano-particles, a number of methods have been used for the production of nano-structured TiO_2 coatings, such as electrophoretic deposition (EPD) [5–7], sol–gel [8,9], thermal spray [10,11], and plasma spray [12,13], etc. Among them, suspension high velocity oxy fuel (SHVOF) thermal spray is an emerging technology for producing dense and nano-structured ceramic coatings with a significant improvement in density, strength and durability over conventional thermally sprayed coatings [14,15]. For SHVOF, modifications on conventional HVOF guns were carried out by replacing the ordinary powder injection system with a suspension injection device with a stirrer [16]. Direct injection of suspensions into the combustion chamber also leads to significant improvement of the heat transfer between the HVOF flame and the fine particles, and results in a more uniform microstructure [17]. Nevertheless, the flame heat power needs to be well-controlled as it would strongly affect the phase stability of nano-TiO_2, which is the key to its photocatalytic properties [18]. TiO_2 generally exists in nature in three polymorphic phases: anatase, rutile, and brookite [19–21]. Anatase phase is less stable than rutile, which irreversibly transfers to rutile at high temperatures (728 °C) [22].

In our previous work [23], a range of nano-structured TiO_2 coatings were prepared by SHVOF from a water-based suspension of pure anatase powders using flame heat powers ranging from 40 kW to 101 kW. It was demonstrated that the heat powers had a significant effect on the phase compositions of the TiO_2 coatings as a mixture of rutile and anatase phases. The rutile content increased exponentially with heat powers, which was believed to be undesirable as previous studies suggested that a higher content of anatase was preferred owing to better photo-activity [24]. Nevertheless, it has also been reported that mixed-phase TiO_2 exhibited even better photocatalytic properties than pure anatase or high anatase content [25,26]. To explain these disagreements, it is essential to look into other factors (e.g. microstructure, crystallite size, etc.) that may also contribute to the distinctive photocatalytic behaviour apart from the phase effect. With this question in mind, in this study, we carried on our previous investigations on the nano-structured TiO_2 coatings sprayed by the SHVOF technique using rutile suspensions. The resulting coating microstructure, mechanical properties, and topography were investigated by scanning electron microscopy (SEM), micro-indentation and surface profilometry. Phase content was analysed using X-ray diffraction

* Corresponding author.
E-mail address: tanvir.hussain@nottingham.ac.uk (T. Hussain).

http://dx.doi.org/10.1016/j.ceramint.2017.08.068
Received 27 June 2017; Received in revised form 8 August 2017; Accepted 9 August 2017
Available online 10 August 2017

(XRD) in combination with Rietveld Refinement. The mechanisms for phase evolution during the SHVOF process with both suspensions of anatase and rutile powders were discussed. Linear sweep voltammetry test (LSV) was used to evaluate the coatings' photocatalytic performance. The correlation between the photocatalytic behaviour of TiO_2 coatings and other coatings' properties was also discussed (e.g. microstructure, phase content, and crystallite size, etc.). We aimed to obtain nano-structured TiO_2 coatings with desirable properties and the most sensitive photo-activity by optimising parameters for suspension HVOF thermal spray.

2. Experimental procedure

2.1. Materials

A commercial water-based rutile suspension (MilliDyne, Finland) with a solid content of 30 wt% was used in this study. The suspension was sprayed onto AISI 304 stainless steels (Fe-19.0Cr-9.3Ni-0.05C in wt%) with dimensions of 60 × 25 × 1.5 mm.

2.2. Spray Process

Substrates were grit blasted with F100 brown alumina particles (0.125–0.149 mm) under 2 bar pressure, and cleaned by an ultrasonic acetone bath to remove any embedded alumina particles. The samples were then mounted onto a carousel rotating at 73 rpm with a vertical axis of rotation. The suspension was mixed for 90 min using mechanical stirrer at a speed of 940 rpm to achieve homogeneous suspension. A modified UTP/Miller Thermal HVOF system with a direct injection at the centre of the gas mixing block was used to spray the suspension. The suspension injector had a diameter of 0.3 mm to inject the suspension into the centre of the combustion chamber. A 22 mm long combustion chamber with 110 mm long barrel nozzle was used in this study. The suspension was fed using a pressurised 2 L vessel equipped with a mechanical stirrer to ensure uniform dispersion of the nanoparticles in solution and consistent flow onto the substrate without clogging of the nozzle. The pressure of the feeding system was fixed at 3 bar during the spray with a flow rate of 80 mL/min. The gun was mounted on a z-axis traverse unit in front of the rotating carousel and it was set to a stand-off distance from the surface of the substrate of 85 mm. The gun was scanned vertically up and down at 5 mm/s to build up a coating of the required thickness. The substrates were cooled by compressed air jets during and after the spray. The flow rates were set using a volume control system for fuel gas and oxygen as shown in Table 1. Hydrogen was used as combustion fuel to achieve a cleaner flame and also to reduce any hydrocarbon combustion products in the resulting coating, as any contamination might affect the photocatalytic behaviour. The theoretical flame heat power for each spray was calculated using standard combustion formulae and the samples are labelled by the flame heat powers throughout the paper.

2.3. Characterisation

A scanning electron microscope (SEM, JEOL JSM-6490LV, USA) operated at 20 kV was used to examine the suspension feedstock powder and the coating microstructure under secondary electron (SE) and back-scattered electron (BSE) modes. Coating thickness and porosity were analysed by Image-pro plus software (Media Cybernetics, USA) using the BSE images from 3 different locations with a total area of 600 × 600 μm^2. The coating roughness was measured by Talysurf CLI 1000 tester (Taylor Hobson, UK). Six profiles (2 mm in length) for each sample were conducted, three along the length, and three along the width of the sample surface area. Micro-hardness testing was carried out on polished cross-sections near the central area of coatings using a Vickers tester (BUEHLER, UK). A loading of 25 gf was applied for 30 s in 10 different regions for each sample. An X-ray diffractometer (XRD, D500 Siemens) was used to analyse the feedstock suspension powder and the as-sprayed coating. The anatase content in the TiO_2 coating is usually quantified by an equation developed by Keller et al. [27] using the intensities of anatase (101) and rutile (110) peaks as follows:

$$C_A = \frac{8I^{A(101)}}{8I^{A(101)}+13I^{R(110)}}\times 100\% \quad (1)$$

When the crystallite size is smaller than 300 nm, XRD peaks are broadened so the use of relative height of XRD peaks in XRD patterns can result in errors. Alternatively, the peak area was used to calculate the anatase content in the TiO_2 coating by the following equation:

$$C_A = \frac{A^{A(101)}}{A^{A(101)}+1.265A^{R(110)}}\times 100\% \quad (2)$$

where C_A is the anatase content in the coating, $A^{R(110)}$ and $A^{A(101)}$ the areas of the rutile (110) peak and the anatase (101) peak respectively [28]. Quantitative Rietveld refinement (TOPAS V5, Bruker) was also employed to analyse the phase composition in coatings, and principles of whole powder pattern modelling (WPPM) were used for crystallite size and micro-strain calculations [29]. The Lotgering factor F(*hkl*) was computed for the three theoretically most intensive rutile reflections of (110), (101) and (211). The Lotgering factor represents a simple qualitative measure to assess whether any preferred orientation in the irradiated volume is present by comparing peak or integral intensities of the measured XRD pattern and those of a randomly oriented powder sample [23]. The comparison is made for the intensity of selected (*hkl*) (I^{hkl}) and the intensities I in a chosen 2θ range in the following manner:

$$F(hkl) = \frac{\frac{I^{hkl}}{\Sigma_{2\theta\ range} I} - \frac{I_0^{hkl}}{\Sigma_{2\theta\ range} I_0}}{1 - \frac{I_0^{hkl}}{\Sigma_{2\theta\ range} I_0}} \quad (3)$$

Lotgering factor of 0 corresponds to a completely random distribution while the value of 1 would indicate a complete orientation of the chosen (*hkl*) planes in the sample. Due to overlap of anatase and rutile reflections in measured XRD patterns, Lotgering factor was computed using peak intensity values after background level subtraction of the measured data and I_0 were taken from rutile powder diffraction PDF 21–1276. The considered rutile reflections in the chosen 2θ range were (110), (101), (200), (111), (210), (211), (220) and (310).

2.4. Photo-activity test

Electrochemical characterisations were carried out using Autolab PGSTAT30 (EcoChemie, Netherlands) in a two-electrode cell with the sample as photo-anode and a platinum wire with a 0.5 mm diameter as counter-electrode. The photocurrent was recorded under the linear sweep voltammetry (LSV) scan starting from the open circuit potential to 1.2 V at a scan rate of 10 V/s. A sacrificial electrolyte (0.28 M Na_2S/ 0.32M Na_2SO_3, Sigma-Aldrich) was used in order to prohibit the backward reactions and the rapid recombination of e^-/h^+ pairs [2]. Experiments were conducted under both light and dark conditions to determine the photocatalytic properties of the prepared samples. A xenon lamp-based Oriel 96000 150 W solar simulator (AM 1.5 G,

Table 1
Gas flow rate and flame heat power.

Coating	H_2 flow rate (L/min)	O_2 flow rate (L/min)	Total flow rate (L/min)	Flame heat power kW
R40	244	122	367	40
R72	438	219	657	72
R101	611	306	917	101

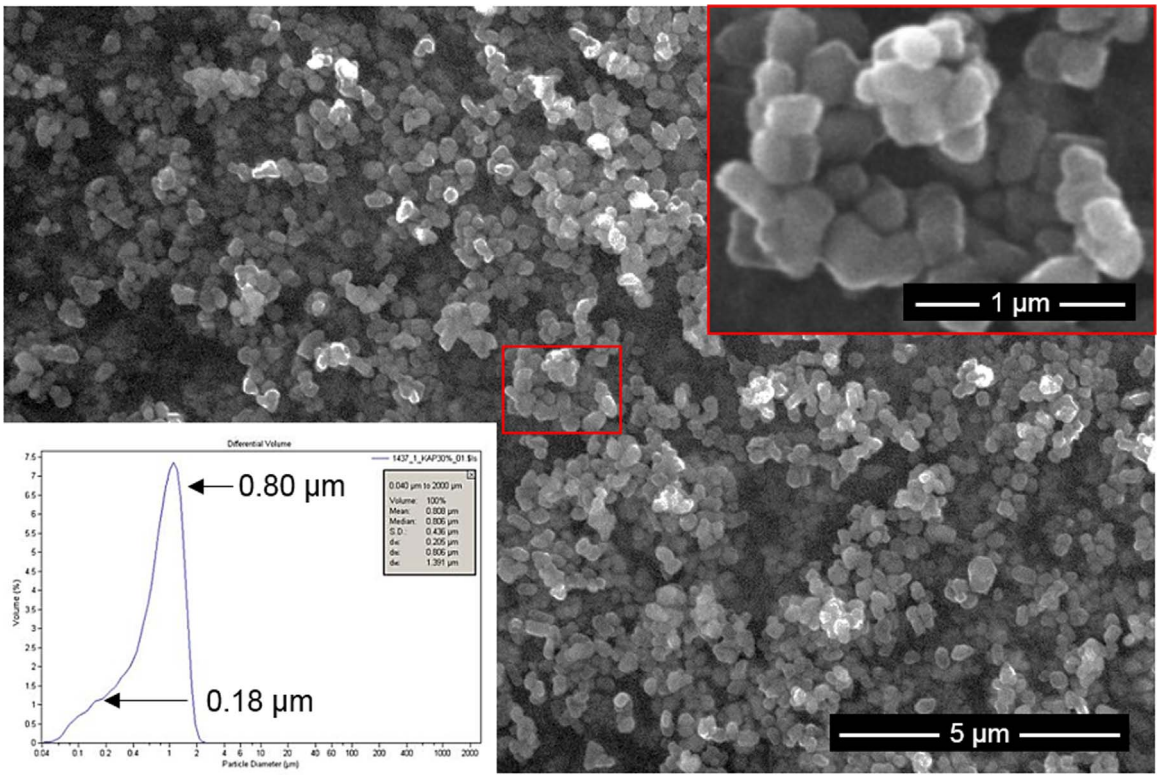

Fig. 1. Secondary electron (SE) images of feedstock rutile TiO_2 particles showing particle morphology and size distributions (laser diffractometry data was provided by the supplier).

100 mW/cm^2) served as the simulated sunlight source and the total percentage of output AM 1.5 G spectrum was 4.1% of UV, 54.7% of visible light and 41.2% of infrared. The samples were cut into a T shape with a coating area of 16 × 12 mm immersed into electrolyte and a long handle (44 × 4 mm) coated with silicone rubber for isolation from the electrolyte. The reaction mechanisms on each electrode can be found in Ref. [30].

3. Results and discussion

3.1. Suspension feedstock

Fig. 1 shows the morphology of the rutile powders dried for 2 h at 100 °C from the suspensions. The particles have a slight angular morphology with an average diameter of ~180 nm. The laser diffractometry data provided by the supplier showed a bimodal size distribution with a median of ~180 nm and another median of ~800 nm. The larger size distribution indicates that rutile nano-particles were slightly agglomerated in the suspension, which could affect the heat transfer during spraying and the resulting coating microstructure.

3.2. Surface morphology

Fig. 2 shows the surface morphology of the as-sprayed coatings using rutile suspensions with different flame powers (R40, R72 and R101). It is obvious that R72 and R101 coatings show distinctive surface topography in compared with the R40 coating. Both coatings appear to have humps that have spherical shapes ranging from 50 to 150 μm in size and distributed uniformly on the surface, while the R40 coating has a smooth surface with no clear humps at all. The surface morphology is analysed by the surface roughness measurement, which is shown in Fig. 3. It shows that the R40 has a relatively lower surface roughness (Ra) as comparable to grit-blasted stainless steel (SS) substrates; while R72 and R101 have much higher roughness with larger deviations than that of R40. The average roughness of R101 is also ~15% higher than that of R72, showing an increasing roughness with flame power.

In addition, higher magnification shows that the R40 surface was built up by mostly individual unmolten nano-particles with a slightly larger particle size than the feedstock as shown in Fig. 1. In comparison, higher flame powers (R72 and R101) resulted in fully melted splats along with humps on the surface, and the microstructure is similar between the area with humps and other flat areas. This difference indicates that the low flame power (R40) yielded less heat transfer from the HVOF flame to the feedstock particles resulting in insufficient energy to fully melt the rutile particles and therefore retained a majority of nano-sized particles.

3.3. Cross-sectional microstructure

Fig. 4 shows the representative cross-sectional microstructure of the as-sprayed coatings under BSE mode. It is observed that R40 has a uniform thickness with a bimodal microstructure that contains fully melted splats (bright area) and un-molten agglomerated nano-particles (dark grey area). With the increase of flame power (R72 and R101), the agglomerated nano-particles disappeared owing to better particle heating. The dark black areas in R72 and R101 correspond to nanoscale porosity in the coatings which are more obvious in hump areas as inter-pass porosity. The occurrence of humps in SHVOF coatings was suggested to be originated from the grit blasted substrate surface [23]. During SHVOF spraying, the sample surface roughness continually changes with each subsequent pass of the spray gun. The accumulation of individual splats as they are piled up in succession will alter the surface roughness for the next pass of the spray gun (For more detailed explanations, see Fig. 9 in Trice and Faber's paper [31]). Fig. 5 shows the average coating thickness and porosity measurements according to the BSE images. It is clear that R101 has the lowest porosity among the three, and the reduced porosity however resulted in the lowest thickness possibly due to more efficient particle flattening on impact. The decreasing trend of coating porosity with higher flame

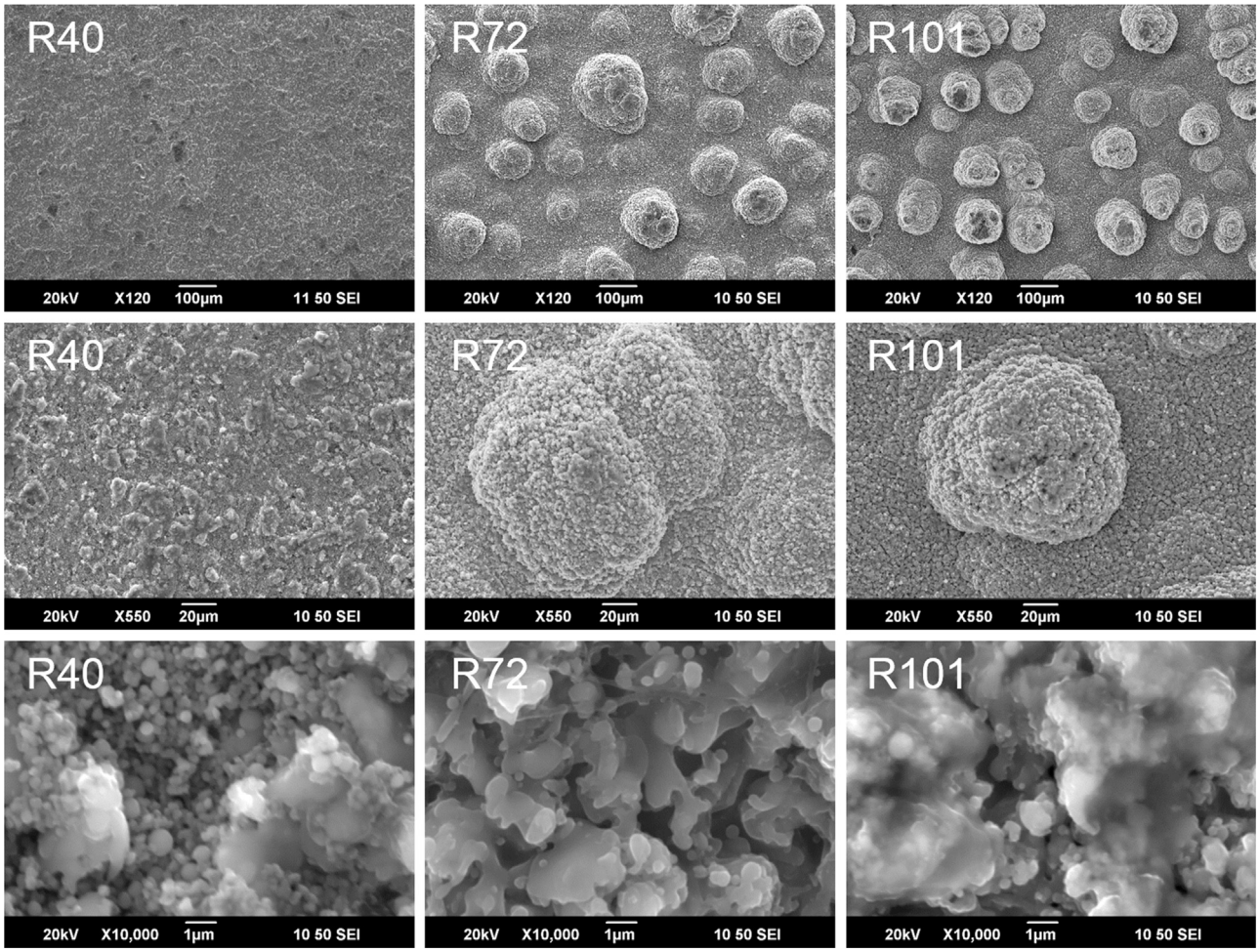

Fig. 2. SE images of the top surface morphologies of the as-sprayed coatings with detailed features as shown in the right column. The emergence of humps at higher flame powers are highlighted with detailed observations from the top surface with higher magnifications.

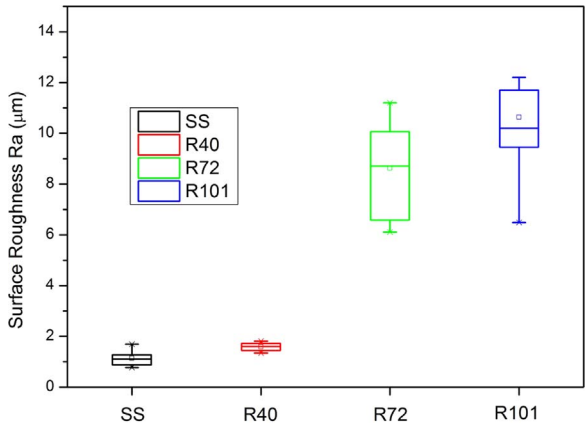

Fig. 3. Box plot of the surface roughness of the stainless steel (SS) and coatings.

power agrees well with the previous study on the SHVOF spray [32].

The integrity of the coating microstructure could also be evaluated by measuring the micro-hardness. Fig. 6 shows the micro-hardness measurements obtained from the central area on the cross-sections of the as-sprayed coatings. There is also an increasing trend with higher flame powers but with huge difference in values. R40 has the lowest average micro-hardness (2.56 ± 0.69 GPa), which is 2 times lower than that of R72 (8.08 ± 1.41 GPa) and 8 times lower than that of R101 (22.75 ± 6.9 GPa). It indicates that the flame powers have a significant effect on coating hardness, for example, applying 101 kW resulted in nearly 10 times the hardness of R40. On the other hand, several measurements on the R101 coatings are as high as 32.5 GPa, which is close to the hardness of the hardest known oxide: cotunnite-structured TiO_2 with a hardness of 38 GPa [33]. These materials were obtained by applying high-pressure (> 60 GPa) and high temperature (1100 K) on rutile or anatase TiO_2. The starting material for this process has in fact gone through similar process with the feedstock materials during the SHVOF spray that were fully-melted and impacted onto the substrate surface by supersonic high particle velocity (up to ~1200 m/s according to Ref. [34]).

3.4. Phase evolution

In general, the rutile phase is more stable than the anatase phase, and the phase transformation at solid state from rutile to anatase is irreversible. However in HVOF spraying, the feedstock particles would be heated to a fully molten or partially molten state before impacting on the substrates and then solidify upon a rapid cooling process (up to 10^6 K/s according to Ref. [28]). Under this condition, the metastable anatase phase then evolved with transformation from the stable rutile. As a result, the spraying parameters of the HVOF process could directly affect the phase content of anatase in the resulting coatings. Fig. 7 shows the quantitative Rietveld refinement results of the XRD patterns of the feedstock suspension dried powders and the as-sprayed coatings highlighting the (101) peak for the anatase phase and the (110) peak for the rutile phase. These two peaks are normally used for quantitative phase composition analysis of TiO_2 coatings according to the Eqs. 1 and 2, which are dedicated to powder samples with the assumption of

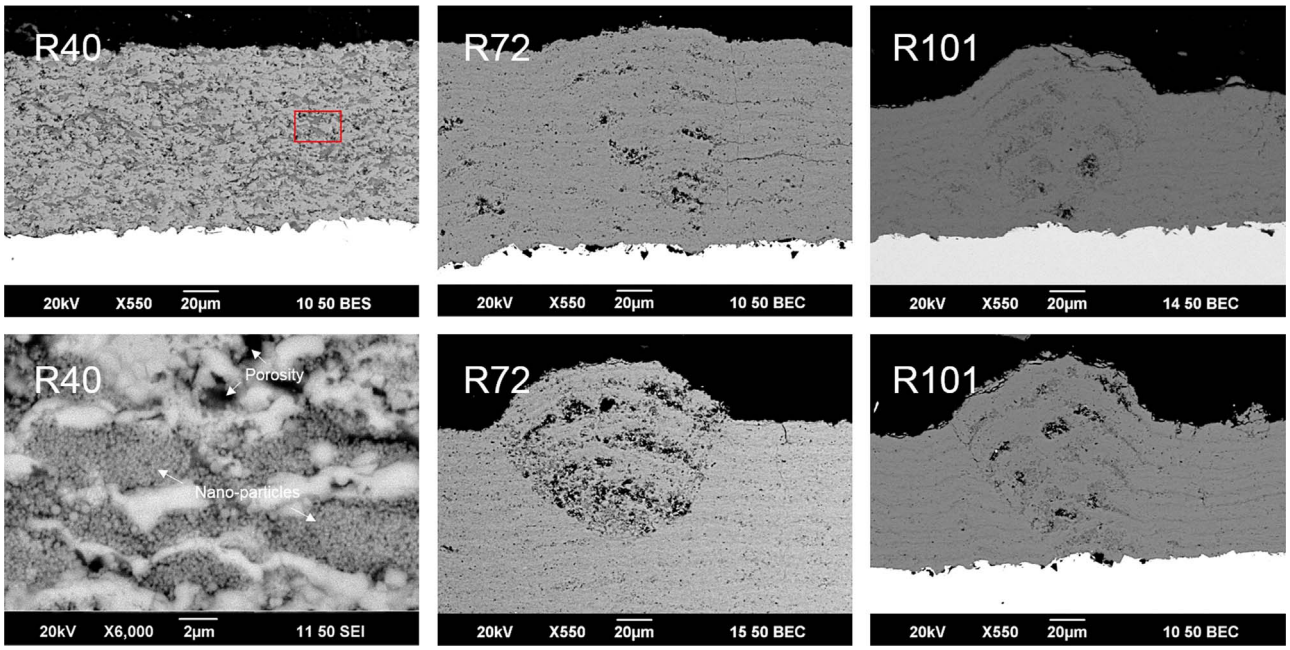

Fig. 4. Back-scattered electron (BSE) images showing the cross-sectional microstructure of the as-sprayed coatings. The emergence of humps at higher flame powers are highlighted showing the presence of voids underneath the humps.

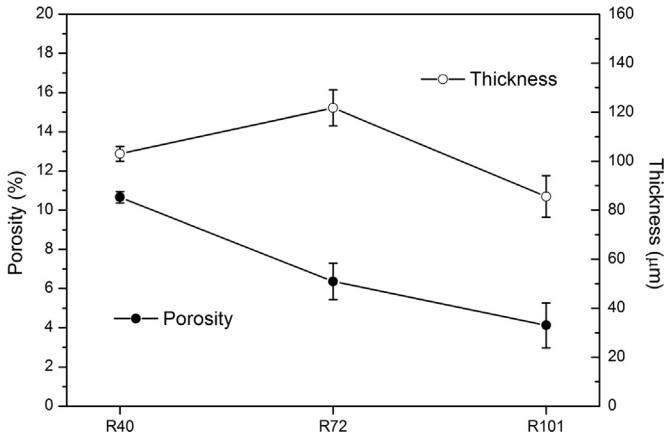

Fig. 5. Plot of the average porosity (left) and thickness (right) of the coatings.

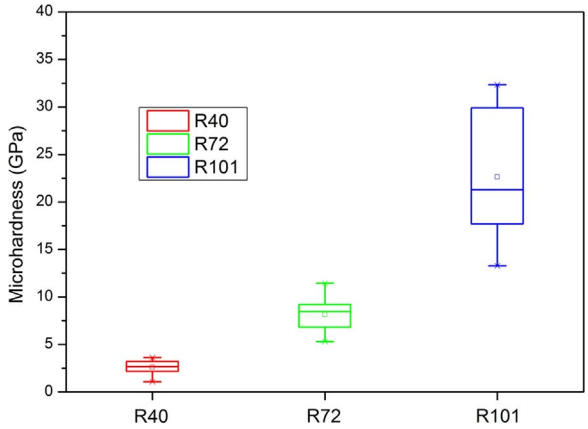

Fig. 6. Box plot of the measurements of micro-hardness of the coatings.

random orientations. Rietveld refinement method is highly preferred for accurate phase composition determination of thermal sprayed coatings [23]. This is mainly because it can take into account the existence of preferred orientation in the thermal sprayed coatings due to the inherent anisotropy of the deposition process.

The quantitative analysis using these three approaches is summarised in Fig. 8. The results all show similar trends but it appears to have a wide variance among three approaches when the flame power is the highest (R101). The anatase content in R101 is only ~25%, which is significantly lower than the values calculated by Eqs. 1 and 2. This is mainly caused by the preferred orientation in the as-sprayed coatings, which can be characterised by Lotgering factors of selected rutile reflections using Eq. (3) (See Fig. 9). The positive values indicate the measured intensity is higher than that in the randomly oriented sample and vice versa [35]. Although it is difficult to correlate the texture in the coatings directly with the processing parameter, it is clear that high flame powers yielded higher degree of deviation from the central line (zero), which means stronger preferred orientation. This strong texture with such a high Lotgering factors (~0.2) was also found in plasma sprayed TiO_2 coatings [36] and the texture became stronger with the increase of flame power.

Fig. 10 plotted the anatase content (Rietveld refinement results) in the SHVOF as-sprayed coatings using rutile powder as a dependency of the flame heat power, in combination with the data from Pala et al. [23] with anatase powders as feedstock. It is obvious that when using anatase powder, the anatase content decreases nearly linearly with the increase of the flame heat power. While coatings using rutile powder are observed to have similar anatase content when the flame heat power is 72 kW or higher. In addition, in both cases, flame heat powers lower than 72 kW resulted in insufficient heat supply for melting the powders and therefore retained mostly the original anatase or rutile phase from the feedstock. It is obvious that the flame heat power has a significant effect on the phase of the SHVOF coatings and the transformation rate from anatase to rutile is an exponential function of temperature [37]. The phase evolution of HVOF TiO_2 coatings deposited with rutile and anatase powders as feedstock was discussed earlier by Li et al. [28] and the data are re-calculated and plotted in Fig. 10 (dashed lines). Li et al. [28] used fuel gas flow instead of flame heat powers, which can be converted using standard combustion formulae and the database of propane.

It is worth noting that the anatase content in Li et al. [28] was obtained by the conventional method using Eq. (2), which failed to consider the significant effect of texture in the HVOF coatings

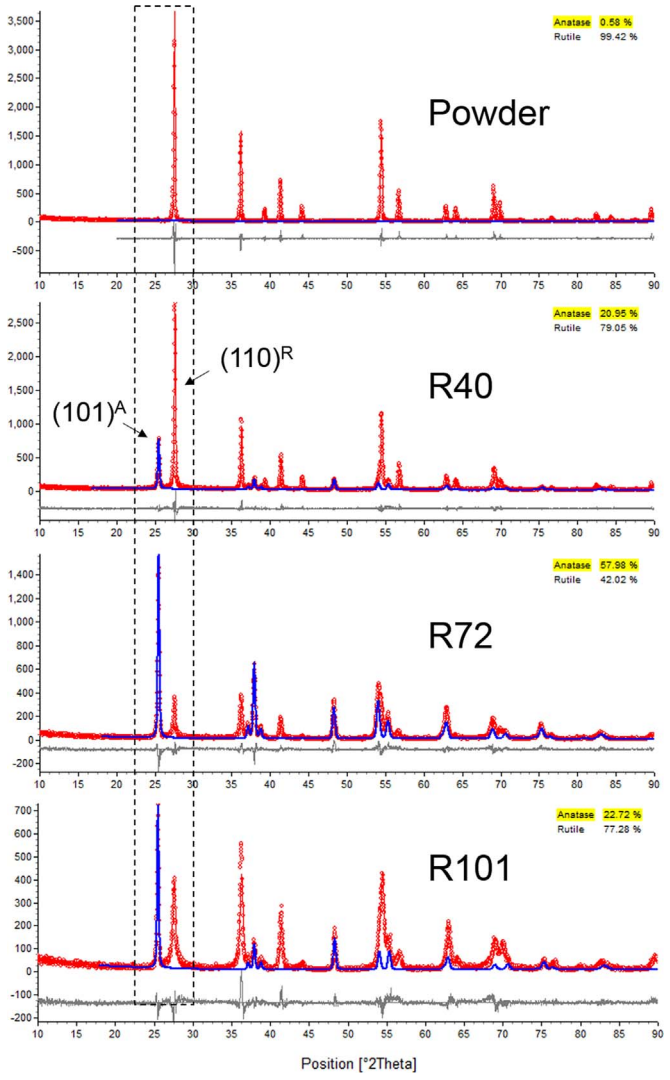

Fig. 7. Rietveld refinement results of the rutile suspension dried powders and as-sprayed coatings showing the phase composition of anatase and rutile. The dashed rectangular is highlighting the (101) peak for anatase phase and (110) peak for rutile phase.

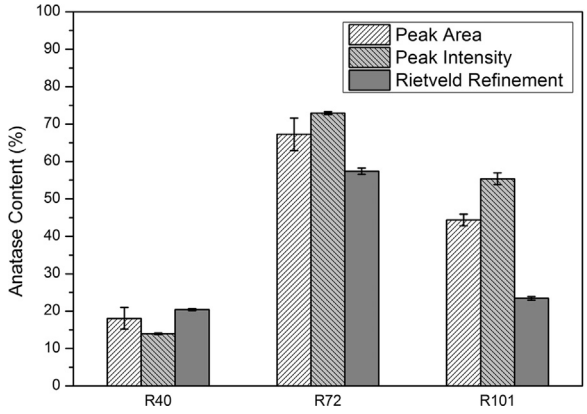

Fig. 8. Histograms of the phase compositions of anatase phase using 3 different methods.

especially using higher flame heat powers as discussed earlier, and therefore may not be as accurate as Rietveld refinement results. In addition, the range of the flame heat power is only limited to less than 72 kW, and powders with different sizes were used instead of suspensions, which might incur insufficient heat transfer to the feedstock

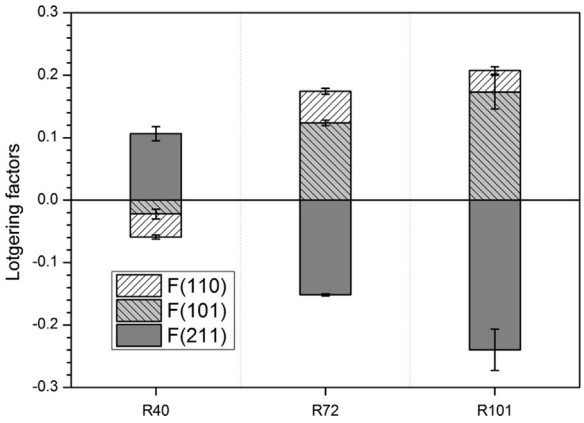

Fig. 9. Histograms of the Lotgering factors for (101), (110) and (211) rutile reflection.

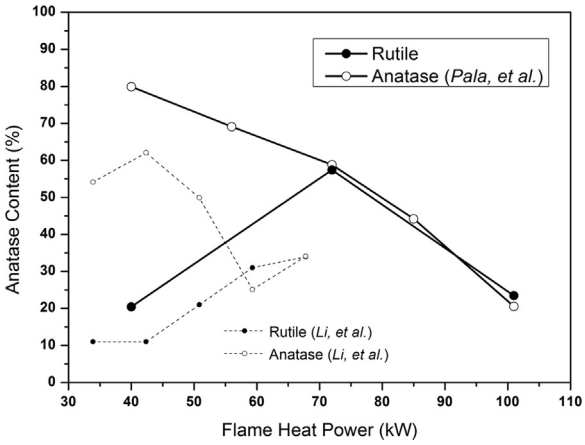

Fig. 10. Plot of the anatase content (Rietveld refinement results) as a dependency of flame heat power (kW) in the as-sprayed SHVOF coatings using rutile powders and anatase powders (data retrieved from Pala et al. [23]) as feedstock. Dashed lines are data from Li et al. [28].

powders during spraying. Nevertheless, a decreasing trend is still observed in the anatase powder while an increasing trend is observed in the rutile powder. The heat power of 72 kW becomes a critical value for the deposition of TiO_2 coatings, above which coatings using both rutile and anatase powders resulted in the same amount of anatase phase. This finding simplified and corrected the phase evolution mechanism of HVOF TiO_2 coatings using rutile and anatase powders as proposed by Li et al. [28]. In both cases above the critical flame power, the feedstock powders are turned into molten droplets by the hot flames, and the anatase phase was then obtained by the same phase transformation from rutile to anatase during the cooling process.

3.5. Photocatalytic behaviour

The photo-electrochemical properties of the coated samples were investigated by measuring the photocurrent density under illumination in a Na_2S/Na_2SO_3 aqueous solution serving as the sacrificial electrolyte. Fig. 11 shows the observed photo-electrochemical behaviour of the three samples of which the sample R40 exhibits the best photo-conversion efficiency in comparison with R72 and R101 as featured by the greatest slope of the LSV (the black photo-current plot). It is known that the photo-conversion efficiency greatly depends on the separation processes of the photo-generated electron-hole pair. Accordingly, at a low applied potential, the separation of electrons and holes can be easier and more rapid for R40 rather than the other samples, leading to a greater current increase. In contrast, variation of the potential on the sample electrode caused little current increase under dark conditions.

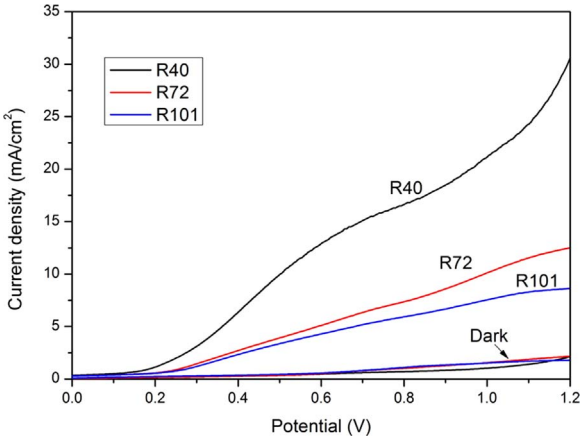

Fig. 11. Photocatalytic behaviour of the coatings under light and dark environment: LSV recorded under light and dark conditions at 10 mV/s potential scan rate.

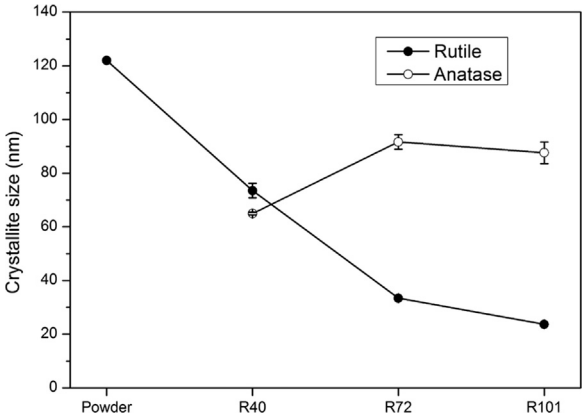

Fig. 12. Plot of the average crystallite size in rutile and anatase of powder and coatings.

Though it is commonly agreed that the photocatalytic activity of TiO_2 mostly results from the anatase phase presented in the sprayed coatings, several authors demonstrated that titania coatings having rutile as the main phase were also photo-catalytically active [38–40]. This agrees with our observations that the sample R40 with high rutile content (79.05%, Fig. 7) was very photoactive. Apart from the effect of phase composition, other factors may affect the photocatalytic activity of TiO_2 as well, such as the presence of defects, surface area [41] and crystallite size [42]. For example, Toma et al. [26] found that using low gas flow can produce a bimodal microstructure consisting of well-melted regions and other regions dominated by nano-sized agglomerated particles, which is similar to the microstructure of R40 as shown in Fig. 4. Such microstructure enabled the high photocatalytic activity comparing to the well-melted coating structure of the other two samples. The presence of these un-melted nano-particles increased the specific surface area of R40, leading to enhanced light absorption, photoexcitation, generation of electron-hole pairs and formation of photoactive radicals (ions) for initiation of the photocatalytic reactions. Although the presence of these un-melted and agglomerated nano-particles can be clearly seen in the high-resolution SEM images it is challenging to quantify their contribution to the overall surface area. Toma et al. [26] studied SHVOF sprayed rutile titania coatings prepared from 500 nm feedstock particles which reportedly had a specific surface area of about 10 m^2/g. It is reasonable to expect the specific surface area of the agglomerated nano-particles in R40 coatings is of similar order of magnitude. The samples with humped rough surfaces (R72 and R101) were grounded into flat surface ($R_a < 5$ μm) and tested. No significant change in the photocatalytic activity was observed, which indicates the effect of increasing the macroscopic surface area by humping the surface is negligible.

On the other hand, rutile has always been considered as a passive electron sink hindering recombination in anatase, and its inactivity is due in part to rapid rates of recombination. In mixed-phase TiO_2, charges produced on rutile under illumination are stabilized through electron transfer to lower energy anatase lattice trapping sites. It was suggested that within mixed-phase titania (anatase+rutile), there is a morphology of nanoclusters containing atypically small rutile crystallites interwoven with anatase crystallites [25]. The transition points between these two phases allow rapid electron transfer from rutile to anatase. Thus, rutile acts as an antenna to extend the photo-activity into visible wavelengths and the structural arrangement of the similarly sized TiO_2 crystallites creates catalytic "hot spots" at the rutile-anatase interface. The average crystallite size of SHVOF coatings using rutile powders is shown in Fig. 12, which shows similar trends with the previous results using anatase powders (See Fig. 10 in Pala et al. [23]). The crystallite size of the rutile phase decreased with the increase of flame heat powers, while the anatase increased at the beginning and then levelled over 72 kW. Also as shown in Fig. 12, higher flame heat powers resulted in larger differences in crystallite sizes between anatase and rutile phases, and therefore failed to take advantage from the above mechanism. While at a low flame power (40 kW), the difference in the crystallite sizes is negligibly small (< 10 nm), leading to the improved photo-activity.

4. Conclusions

The SHVOF thermal spray technique was applied to spray photocatalytically active titania coatings starting from the commercially available submicron rutile suspension with three different flame powers of 40, 72 & 101 kW. All the coatings experienced phase transformation from stable rutile to metastable anatase, and all exhibited photocatalytic activity. It was found that the flame powers played significant effects on the coatings' microstructure, mechanical properties and the phase evolution; and several conclusions can be drawn as follows:

1. Using low flame heat power of 40 kW produced a bimodal microstructure consisting of un-melted nanoparticles and fully melted splats. It had the highest porosity (~11%), lowest micro-hardness (~3 GPa), roughness (R_a ~2 μm) and anatase content (~20%). It somehow exhibited the highest photocatalytic activity, which was suggested to be due to the increased specific surface area of the un-melted nano-particles. More importantly, the structural arrangement of the similarly sized TiO_2 nano-crystallites (rutile ~65 nm; anatase ~75 nm) creates catalytic "hot spots" at the rutile–anatase interface, in which case, rutile acts as an antenna to extend the photo-activity into visible wavelengths, and therefore improved the photo-activity.
2. Using high flame heat powers of 72 & 101 kW resulted in denser coatings (porosity 5–7%), increased micro-hardness (9–22.5 GPa) and rougher surfaces (R_a: 9–10 μm) with distinctive humps. The effect of flame power on the phase content of coatings prepared from rutile suspensions was the same as coatings with anatase suspensions. Both feedstocks were melted over the critical flame power (72 kW) and experienced the same phase transformation during the spray. The rutile content in the coatings is an exponential function of flame power: the anatase content for 72 kW is the highest (~ 60%) and for 101 kW is only ~25%.

Acknowledgements

This work was supported by the Engineering and Physical Sciences Research Council [grant number EP/MO1536X/1]. The authors acknowledge Al-Shihabi Al-Ani Athil for the repeat measurements of photocatalytic behaviour and Mr. Rory Screaton for the experimental assistance.

References

[1] X. Chen, S.S. Mao, Titanium dioxide nanomaterials: synthesis, properties, modifications, and applications, Chem. Rev. 107 (7) (2007) 2891–2959.
[2] M. Ni, et al., A review and recent developments in photocatalytic water-splitting using TiO2 for hydrogen production, Renew. Sustain. Energy Rev. 11 (3) (2007) 401–425.
[3] S.M. Gupta, M. Tripathi, A review of TiO2 nanoparticles, Chin. Sci. Bull. 56 (16) (2011) 1639.
[4] V. Ducman, V. Petrovič, S.D. Škapin, Photo-catalytic efficiency of laboratory made and commercially available ceramic building products, Ceram. Int. 39 (3) (2013) 2981–2987.
[5] J. Esmaeilzadeh, et al., Dispersant-assisted low frequency electrophoretically deposited TiO2 nanoparticles in non-aqueous suspensions for gas sensing applications, Ceram. Int. 38 (7) (2012) 5613–5620.
[6] H. Farnoush, et al., A kinetic study on the electrophoretic deposition of hydroxyapatite–titania nanocomposite based on a statistical approach, Ceram. Int. 38 (8) (2012) 6753–6767.
[7] A.A. Sadeghi, et al., Electrophoretic deposition of TiO2 nanoparticles in viscous alcoholic media, Ceram. Int. 39 (7) (2013) 7433–7438.
[8] C. Bogatu, et al., Ultrasound assisted sol-gel TiO2 powders and thin films for photocatalytic removal of toxic pollutants, Ceram. Int. 43 (11) (2017) 7963–7969.
[9] V. Tajer-Kajinebaf, H. Sarpoolaky, T. Mohammadi, Sol–gel synthesis of nanostructured titania–silica mesoporous membranes with photo-degradation and physical separation capacities for water purification, Ceram. Int. 40 (1) (2014) 1747–1757.
[10] R.S. Lima, B.R. Marple, thermal spray coatings engineered from nanostructured ceramic Agglomerated powders for Structural, thermal barrier and biomedical applications: a review, J. Therm. Spray. Technol. 16 (1) (2007) 40–63.
[11] F.L. Toma, et al., Comparative study on the photocatalytic behaviour of titanium oxide thermal sprayed coatings from powders and suspensions, Surf. Coat. Technol. 203 (15) (2009) 2150–2156.
[12] Z. Yi, et al., Photocatalytic performance and microstructure of thermal-sprayed nanostructured TiO2 coatings, Ceram. Int. 34 (2) (2008) 351–357.
[13] M.C. Bordes, et al., Preparation of feedstocks from nano/submicron-sized TiO2 particles to obtain photocatalytic coatings by atmospheric plasma spraying, Ceram. Int. 40 (10) (2014) 16213–16225.
[14] A. Killinger, R. Gadow, High velocity thermal spraying of powders and suspensions containing micron, submicron and nanoparticles for functional coatings, Key Eng. Mater. 533 (2012) 99–114.
[15] J. Rauch, et al., Advances in high velocity suspension flame spraying (HVSFS), Surf. Coat. Technol. 203 (15) (2009) 2131–2138.
[16] A. Killinger, et al., Review of new developments in suspension and solution precursor thermal spray processes, J. Therm. Spray. Technol. 20 (4) (2011) 677–695.
[17] F.-L. Toma, et al., Microstructures and functional properties of suspension-sprayed Al2O3 and TiO2 coatings: an overview, J. Therm. Spray. Technol. 19 (1–2) (2009) 262–274.
[18] H. Zhang, J.F. Banfield, Structural characteristics and mechanical and thermodynamic properties of nanocrystalline TiO2, Chem. Rev. 114 (19) (2014) 9613–9644.
[19] A. Beltran, L. Gracia, J. Andres, Density functional theory study of the brookite surfaces and phase transitions between natural titania polymorphs, J. Phys. Chem. B 110 (46) (2006) 23417–23423.
[20] D. Reyes-Coronado, et al., Phase-pure TiO2 nanoparticles: anatase, brookite and rutile, Nanotechnology 19 (14) (2008) 145605.
[21] M. Dawson, C. Ribeiro, M.R. Morelli, Rutile supported anatase nanostructured films as photocatalysts for the degradation of water contaminants, Ceram. Int. 42 (1) (2016) 808–819.
[22] C.-L. Wang, et al., Kinetics of anatase transition to rutile TiO2 from titanium dioxide precursor powders synthesized by a sol-gel process, Ceram. Int. 42 (11) (2016) 13136–13143.
[23] Z. Pala, et al., Suspension high velocity oxy-fuel spraying of TiO2: a quantitative approach to phase composition, J. Eur. Ceram. Soc. 37 (2) (2017) 801–810.
[24] K. Tanaka, M.F.V. Capule, T. Hisanaga, Effect of crystallinity of TiO2 on its photocatalytic action, Chem. Phys. Lett. 187 (1) (1991) 73–76.
[25] D.C. Hurum, et al., Explaining the enhanced photocatalytic activity of Degussa P25 mixed-phase TiO2 using EPR, J. Phys. Chem. B 107 (19) (2003) 4545–4549.
[26] F.-L. Toma, et al., Parameters Influencing the Photocatalytic Activity of Suspension-Sprayed TiO2 Coatings, J. Therm. Spray. Technol. 23 (7) (2014) 1037–1053.
[27] N. Berger-Keller, et al., Microstructure of plasma-sprayed titania coatings deposited from spray-dried powder, Surf. Coat. Technol. 168 (2–3) (2003) 281–290.
[28] C.J. Li, et al., Phase formation during deposition of TiO2 coatings through high velocity oxy-fuel spraying, Mater. Trans. 47 (7) (2006) 1690–1696.
[29] P. Scardi, M. Leoni, Whole powder pattern modelling, Acta Crystallogr. Sect. A: Found. Crystallogr. 58 (2) (2002) 190–200.
[30] H.-T. Chang, High-efficiency photochemical water splitting of CdZnS/CdZnSe nanostructures, J. Mater. 2013 (2013).
[31] R.W. Trice, K. Faber, Role of lamellae morphology on the microstructural development and mechanical properties of small-particle plasma-sprayed alumina, J. Am. Ceram. Soc. 83 (4) (2000) 889–896.
[32] P. Ctibor, M. Hrabovský, Plasma sprayed TiO2: the influence of power of an electric supply on particle parameters in the flight and character of sprayed coating, J. Eur. Ceram. Soc. 30 (15) (2010) 3131–3136.
[33] L.S. Dubrovinsky, et al., Materials science - the hardest known oxide, Nature 410 (6829) (2001) 653–654.
[34] A. Killinger, P. Müller, R. Gadow, What do we know, what are the current limitations of suspension HVOF spraying?, J. Therm. Spray. Technol. 24 (7) (2015) 1130–1142.
[35] R.J. Ong, D.A. Payne, N.R. Sottos, Processing effects for integrated PZT: residual stress, thickness, and dielectric properties, J. Am. Ceram. Soc. 88 (10) (2005) 2839–2847.
[36] J. Li, C. Ding, Crystalline orientation of plasma-sprayed TiO2 coatings, J. Mater. Sci. Lett. 17 (20) (1998) 1747–1749.
[37] D.A. Hanaor, C.C. Sorrell, Review of the anatase to rutile phase transformation, J. Mater. Sci. 46 (4) (2011) 855–874.
[38] P. Ctibor, et al., Plasma sprayed TiO2: the influence of power of an electric supply on relations among stoichiometry, surface state and photocatalytic decomposition of acetone, Ceram. Int. 38 (4) (2012) 3453–3458.
[39] C. Zhang, et al., Effect of porosity on photocatalytic activity of plasma-sprayed TiO2 coating, J. Therm. Spray. Technol. 22 (7) (2013) 1193–1200.
[40] E. Bannier, et al., Microstructure and photocatalytic activity of suspension plasma sprayed TiO2 coatings on steel and glass substrates, Surf. Coat. Technol. 206 (2) (2011) 378–386.
[41] G. Tian, et al., Preparation and characterization of stable biphase TiO2 photocatalyst with high crystallinity, large surface area, and enhanced photoactivity, J. Phys. Chem. C. 112 (8) (2008) 3083–3089.
[42] J.C. Yu, et al., Effects of F-doping on the photocatalytic activity and microstructures of nanocrystalline TiO2 powders, Chem. Mater. 14 (9) (2002) 3808–3816.